Hartmann Testing of X-Ray Telescopes

Timo T. Saha[a], Michael Biskasch[b], William W. Zhang[a]

[a]NASA/Goddard Space Flight Center, 8800 Greenbelt Road, Greenbelt, MD 20771

[b]SGT, Inc, 7701 Greenbelt Road Suite 400, Greenbelt MD 20770

ABSTRACT

Hartmann testing of x-ray telescopes is a simple test method to retrieve and analyze alignment errors and low-order circumferential errors of x-ray telescopes and their components. A narrow slit is scanned along the circumference of the telescope in front of the mirror and the centroids of the images are calculated. From the centroid data, alignment errors, radius variation errors, and cone-angle variation errors can be calculated. Mean cone angle, mean radial height (average radius), and the focal length of the telescope can also be estimated if the centroid data is measured at multiple focal plane locations.

In this paper we present the basic equations that are used in the analysis process. These equations can be applied to full-circumference or segmented x-ray telescopes. We use the Optical Surface Analysis Code (OSAC) to model a segmented x-ray telescope and show that the derived equations and accompanying analysis retrieves the alignment errors and low order circumferential errors accurately.

Keywords: X-ray optics, x-ray mirrors, mirror alignment, wavefront sensing

1. INTRODUCTION

In the x-ray wavelength region, light can be reflected efficiently only at very large angles of incidence. Depending on the wavelength, the grazing angle on the surface may be only about a degree or less. This fact forces the mirrors to be axially long surfaces of revolution. The entrance and exit apertures of the telescopes are very narrow annuli. Wolter type-1 mirrors are typically used for most x-ray astrophysics applications. Wolter type-1 telescopes consist of paraboloidal primary mirror followed by a confocal hyperboloidal secondary mirror.

Highly nested x-ray telescopes are typically segmented into quadrants or multiple segments around the circumference of the telescope. Mirror segmentation is driven by fabrication and mirror assembly considerations. The segmentation further complicates the system image analysis.

The Next Generation X-Ray Optics (NGXO) project and International X-Ray Optics (IXO) projects at Goddard Space Flight Center have developed x-ray and visible Hartmann tests suitable for segmented grazing incidence telescopes and their components[1-3]. In these tests, a narrow slit is scanned in front of the mirror segment across the azimuthal range of the mirrors. Centroid coordinates of the images are calculated. The Half Power Diameter (HPD) and Root Mean Square diameter (RMSD) of centroids are used as evaluation metrics.

The image characteristics of x-ray telescopes are unique and fundamentally different from normal incidence telescopes. The radial cones of light emerging from the mirrors are very narrow radially. Therefore, out-of-focus images tend to be very narrow toroids. The angular width of the toroid can be just a few arc-seconds. These narrow images and their radial centroids measured at several focal plane locations can reveal a wealth of information about the alignment errors and

circumferential errors of the mirrors[4]. The centroid data of Hartmann tests of the Wolter telescopes can be difficult to interpret because the errors from the primary mirror and secondary mirror cannot be separated. A more practical approach is to analyze the errors of the primary and secondary individually before attempting to evaluate the system errors.

In this paper we review the effects of alignment errors of segmented mirrors and their transverse ray equations. We present a process of removing decentering errors from out-of-focus images without knowing the location of the optical axis. We also present the equations that can be used to evaluate the mirror alignment errors, average radius errors, cone-angle errors, and cone-angle variations along the azimuth of the mirrors. Finally, we show how to apply this process to primary and secondary mirrors of segmented Wolter type-1 telescopes.

2. SURFACE EQUATIONS OF WOLTER TELESCOPES

A cross-section of the primary or secondary geometry of a Wolter type-1 telescope is illustrated in Figure 1. The parameter h_0 represents the surface radial height at the axial mid-point of the surface, and L is the axial focal length. The surface equation of the primary parabola or secondary hyperbola can be expressed conveniently using just a single equation[5]:

$$h = \sqrt{h_0^2 + 2\,K\,z - P\,z^2}, \tag{1}$$

where h is the radial coordinate of the mirror, z is the axial coordinate of the mirror, and K and P are constants. This equation is used in the OSAC program[5].

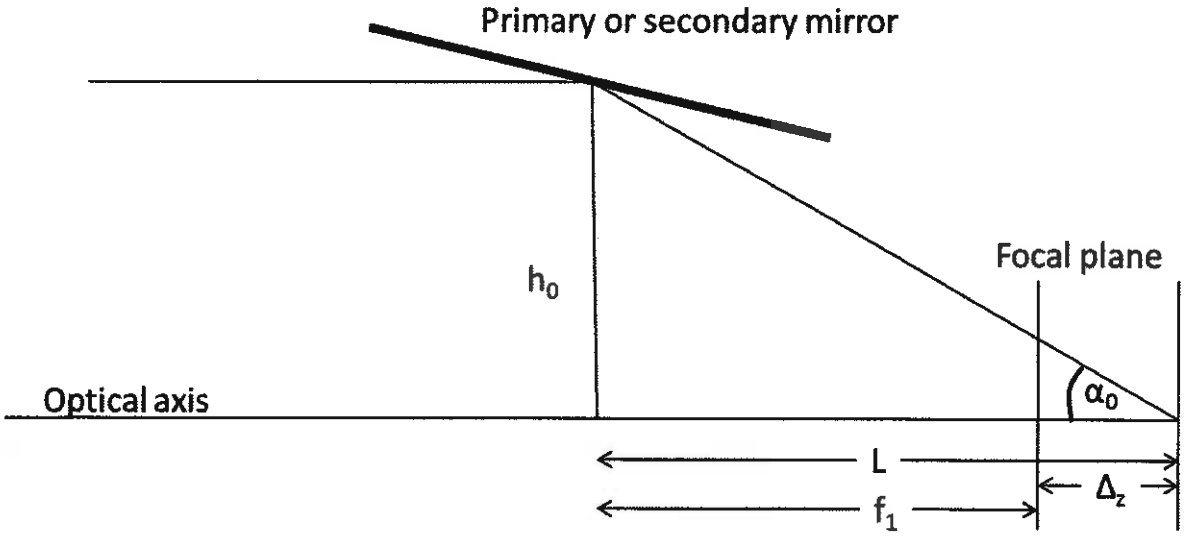

Figure 1. Cross-section of the primary or secondary mirror of a Wolter type-1 telescope.

3. MODELING AND RETRIEVAL OF ERRORS

In the assembly and alignment process of grazing incidence telescopes, primary and secondary mirror segments are first bonded to a temporary mount and then transferred to a permanent mirror mount or module[1]. During the bonding process the alignment and azimuthal shape of the mirror is monitored using an optical Hartmann test. The x- and y-centroids calculated from the Hartmann test are then used to assess and evaluate the process. This process is done first for the primary mirror, then for the secondary mirror, and finally for the combination of the mirrors.

From the centroid data of the Hartmann tests, alignment errors and mirror parameters and their errors can be determined. Alignment errors of mirror segments can be determined from a single Hartmann test. Cone angle errors and average radius errors of mirrors can be evaluated from two or more out-of-focus Hartmann tests.

3.1. CENTROID ERRORS

Ray equations of alignment errors, average radius errors, and delta-radius errors have been derived for the primary and secondary mirrors of Wolter telescopes[6]. Focal plane displacement (Δ_z) is the simplest mirror error. If the focal plane is moved a distance Δ_z from its nominal position, then image centroids of this error can be expressed as a function of azimuth angle, β, and back angle, α_0, as[6]:

$$H_x = \Delta_z \tan(\alpha_0) \sin(\beta) \tag{2}$$

$$H_y = \Delta_z \tan(\alpha_0) \cos(\beta). \tag{3}$$

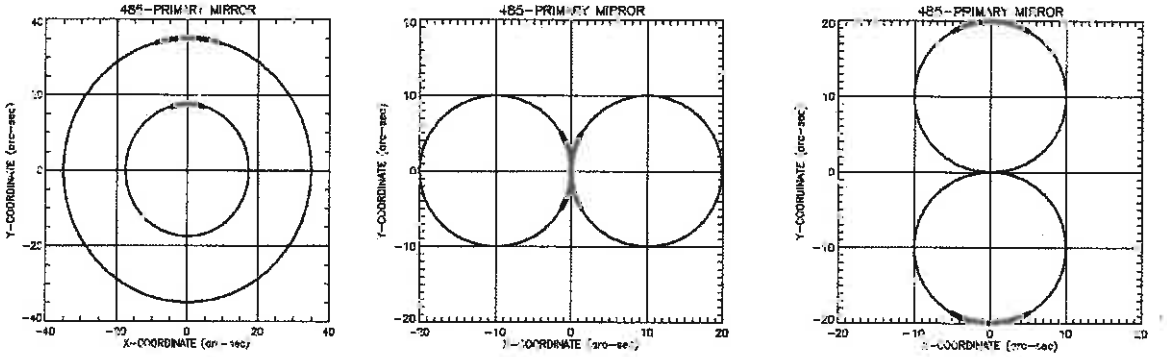

Figure 2. Graphs show the effects of defocus (on the left), azimuth alignment error (in the center), and elevation alignment error (on the right) for a segmented and full revolution mirror. Alignment errors are shown for ±10 arc-sec of error.

If the mirror is segmented, the centroids form an arc with an angular length matching the angular length of the mirror segment. The shape of the resulting images of segmented and full-circumference mirrors are illustrated in Figure 2.

The azimuth alignment error (δ_x) of the mirror rotates the mirror about the y-axis in the x-z-plane. The approximate centroid equations of the error are:

$$H_x = f_1\delta_x - f_1\delta_x\cos(2\beta) \tag{4}$$

$$H_y = f_1\delta_x\sin(2\beta), \tag{5}$$

where f_1 is the distance from the center of the mirror to the location of the detector as shown in Figure 1. The centroids draw an off-centered arc as illustrated in Figure 2. The angular length of the arc is twice the angular length of the mirror segments.

The elevation alignment error, δ_y, of the mirror is generated by rotating the mirror segment about the x-axis in y-z plane. The approximate centroid equations are[6]:

$$H_x = f_1\delta_y\sin(2\beta) \tag{6}$$

$$H_y = f_1\delta_y + f_1\delta_y\cos(2\beta). \tag{7}$$

In this case the centroids generate an off-centered arc and the angular length of the arc is twice the angular length of the mirror. Positive and negative errors generate opposite arcs as illustrated in Figure 2.

Decenter errors of a single mirror do not have the 2β-dependency. Decenter simply translates the mirror segment away from the optical axis. The coordinates of this error are simply:

$$H_x = x_0 \tag{8}$$

$$H_y = y_0, \tag{9}$$

where x_0 and y_0 are the focal plane displacements. The decenter of the secondary mirror with respect to the primary would have the 2β-dependency[4].

The x- and y-centroids of the average radius error can be approximated with equations[6]:

$$H_x = d_0 \sin(\beta) \tag{10}$$

$$H_y = d_0 \cos(\beta), \tag{11}$$

where d_0 is the average radius error. This error simply adds a constant amount of error in every radial location on the surface.

Centroid locations of the delta-radius error, also known as cone-angle error, can be approximately expressed as[6]:

$$H_x = f_1 d_1 \sin(\beta) \tag{12}$$

$$H_y = f_1 d_1 \cos(\beta), \tag{13}$$

where d_1 is the cone-angle error expressed in radians.

Assuming the errors are small, the component of the centroids can be simply expressed as a linear combination of individual terms. Under this approximation the centroid coordinates are:

$$H_x = x_0 + (d_0 + f_1 d_1 + \Delta_z \tan(\alpha_0))\sin(\beta) + f_1 \delta_x + f_1 \delta_y \sin(2\beta) - f_1 \delta_x \cos(2\beta) \tag{14}$$

$$H_y = y_0 + (d_0 + f_1 d_1 + \Delta_z \tan(\alpha_0)) \cos(\beta) + f_1 \delta_y + f_1 \delta_x \sin(2\beta) + f_1 \delta_y \cos(2\beta). \tag{15}$$

These equations can be manipulated into more convenient expressions (H_{PLUS} and H_{MINUS}) using relations:

$$H_{PLUS} = H_x \sin(\beta) + H_y \cos(\beta) \tag{16}$$

$$H_{MINUS} = H_x \cos(\beta) - H_y \sin(\beta). \tag{17}$$

Equation (16) is simply the radial component of the centroids and Equation (17) is the circumferential component of the centroids. These equations can be rewritten by substituting centroids H_x and H_y of the ray equations (14) and (15). After substitution we get for H_{PLUS} and H_{MINUS}:

$$H_{PLUS} = x_0 \sin(\beta) + y_0 \cos(\beta) + (d_0 + f_1 d_1 + \Delta_z \tan(\alpha_0)) + 2 f_1 \delta_x \sin(\beta) + 2 f_1 \delta_y \cos(\beta) \tag{18}$$

$$H_{MINUS} = x_0 \cos(\beta) - y_0 \sin(\beta). \tag{19}$$

The circumferential component (19) is a function of azimuth angle β and translations x_0 and y_0 only. This component does not depend on the alignment terms, average radius error, or cone angle error.

3.2. RETRIEVAL OF ERRORS FROM CENTROID DATA

Centroid equations (18) and (19) provide a basis to estimate the magnitude of all error terms included in the equations. If the azimuth angle β and the centroid coordinates are known, H_{MINUS} and H_{PLUS} can be calculated from equations (18) and (19). Least-squares fitting routines can be used to estimate x_0 and y_0 of equation (19). This process conveniently finds the optical axis. There is no need to locate the optical axis experimentally far away from the mirror segment and the Hartmann scans can be done at several axial locations without moving the detector exactly along the optical axis.

After the centering parameters x_0 and y_0 are calculated, the alignment errors δ_x and δ_y can be estimated from the radial component (18). A least-squares fitting routine is used to fit the constant term (c_1), sin(β)-term, and cos(β)-term of Equation (18) to H_{radial} which is calculated from measured centroid data.

$$H_{RADIAL} = H_{PLUS} - x_0 \sin(\beta) - y_0 \cos(\beta) = c_1 + c_2 \sin(\beta) + c_3 \cos(\beta). \quad (20)$$

In Equation (20) c_1 is substituted for $d_1 + f_1\, d_1 + \Delta_z\, tan(\alpha_0)$, c_2 and c_3 are substituted for $2f_1\delta_x$ and $2f_1\delta_y$, respectively.

The alignment errors δ_x and δ_y can now be estimated from the c_2 and c_3 parameters of the fitting routine. In the equation f_1 is the distance from the axial center of the mirror segment to the detector as illustrated in Figure 1. In order to calculate the centroid coordinates and alignment errors δ_x and δ_y, the azimuth angle β and focal distance f_1 need to be measured.

Fitting parameter c_1 includes the average radius error, cone angle error, and defocus term. These terms cannot be separated and calculated from a single focal plane Hartmann scan. A minimum of two measurements is required. Assuming that fitting of Equation (20) returns parameter c_{11} for centroid data measured at focal distance f_1 and c_{12} at focal distance f_2, then d_1 can be calculated from the equation:

$$d_1 = c_{11} - c_{12} - (f_1 - f_2)\tan(\alpha_0)/f_1, \quad (21)$$

where α_0 is the angle the central ray makes with the optical axis. The cone-angle error of the mirror is now half of the angular error d_1.

After d_1 is estimated, the average radius error is estimated from fitting parameters c_{11} or c_{12}. Knowing the design parameters h_0 and L of the mirror segment, then the average radius error can be written:

$$d_0 = c_{11} - d_1 f_1 - (f_1 - L)\tan(\alpha_0) = c_{12} - d_1 f_2 - (f_2 - L)\tan(\alpha_0). \quad (22)$$

In the case where the mirror parameters L and α_0 are not known, these parameters can be estimated from Equations (21) and (22). Assuming the cone angle error d_1 and average radius error d_0 are zero, Equations (21) and (22) can be solved for L and α_0 parameters.

4. MODELING AND RETRIEVAL OF PRIMARY AND SECONDARY MIRROR ERRORS

The Optical Surface Analysis Code (OSAC)[5] was used to model the Hartmann scan and retrieval process of the alignment errors, average radius errors, and cone-angle errors of the primary and secondary mirrors a Wolter type-1 telescope. In the OSAC environment, surface deformations can be easily modeled using Legendre-Fourier (L-F) polynomials[7]. Design parameters of the modeled telescope are given in Table 1. The mirrors are 30-degree segments of full revolution.

Table 1. Design parameters and dimensions of the modeled telescope.

	Primary	Secondary
P	0.0	-4.17316d-04
K	-1.75273	-5.20717
Mirror radial height h0 (mm)	243.616	240.0193
Mirror axial length Lp (mm)	200.000	200.000
Focal length L (mm)	16929.5	5529.1

The modeling presented in this paper is based on the ray trace only. We are assuming that centroiding of the image data largely removes the diffraction characteristics of the image. An OSAC ray-trace model was built using the data of Table 1. Ray files of the OSAC software are conveniently organized into ray-intercept data as a function of entrance aperture coordinates. These files contain all the data needed to model the primary and secondary mirrors separately, and in combination. From the ray files, one can calculate the image plane centroid data at arbitrary locations in the image space. In the examples we selected 4 image plane displacements. The detector was placed 0.0 mm, −100mm, −200 mm, and −300 mm away from the focus of the mirror towards the optical component.

4.1. MODELING OF PRIMARY MIRROR

Numerical values of errors used in the modeling of the primary mirror are given in Table 2. Cone-angle variation is modeled using the 29th Legendre-Fourier cosine term:

$$L - F_{29} = constant\ z\ cos(29\beta), \tag{23}$$

where z is the axial coordinate and β is the azimuthal coordinate of the deformation. The contour plot of the deformation is shown in Figure 3.

The deformation has 3 maxima and minima across the azimuth and the axial component of the deformation is the 1st order Legendre term.

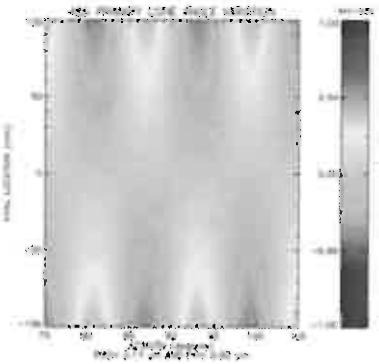

Figure 3. Surface cone angle error of the primary mirror

In Figure 4 the x- and y-centroids of the focal plane images are shown. The centroids are calculated at 4 focus locations (0 mm, −100 mm, −200 mm, and −300 mm). Dashed curves represent centroids if the detector is perfectly centered on the optical axis. The solid curves represent centroids if the detector is not centered on the optical axis.

Table 2. Primary mirror errors and retrieved errors

	Errors introduced	Errors retrieved
Elevation alignment error (arc-sec)	-20.00	-20.00
Azimuth alignment error (arc-sec)	-5.00	-5.01
Average radius error (mm)	0.100	0.101
Cone angle error (arc-sec)	20.63	20.62
Cone angle variation (arc-sec, PV)	0.81	0.81

Images tend to get horizontally longer when moving away from the focus. If the image is elongated vertically, then azimuthal alignment error is dominating. If the image is long horizontally there are two options: either the detector is out of focus or the elevation alignment error is the dominating error. The oscillating waviness in the image is from the cone-angle variation error.

In Figure 5 the circumferential components (H_{MINUS}) are plotted as a function of the azimuth angle. Tilt and vertical displacement of these curves are proportional to the horizontal and vertical decentering of the detector. Decentering parameters x_0 and y_0 are solved for using the fitting process outlined in Section 3.2.

Figure 6 plots the radial component of the centroids as a function of azimuth location. The curves are equally spaced. There is slight tilt in the curves, due to the azimuthal alignment error. A slight 2nd-order sag of the image is coming from the elevation alignment error. The waviness is caused by the cone-angle variation. It is interesting to notice that even a small amount of axial cone-angle error tends to dominate the radial centroid components.

Fitting the centroid data of the radial component H_{RADIAL} in Equation (20) yields the alignment terms if the distance f_1 from the detector to the axial center of the mirror is known. The alignment terms can be calculated for every detector location.

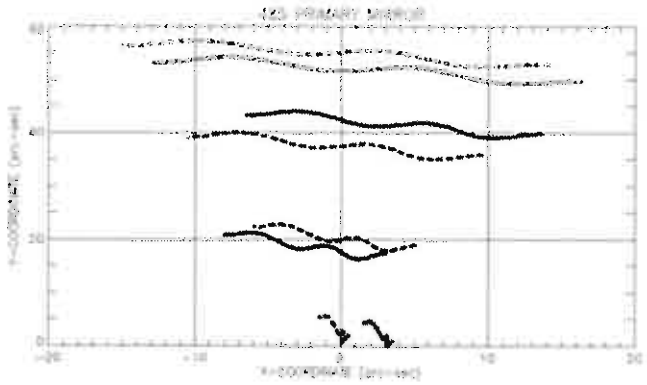

Figure 4. Centroids of 4 Hartmann scans at 0 mm, ±100, mm, ±200 mm, and ±300 mm from the focus. Dashed curves represent centered detector centroids and solid curve represents randomly decentered detector centroids.

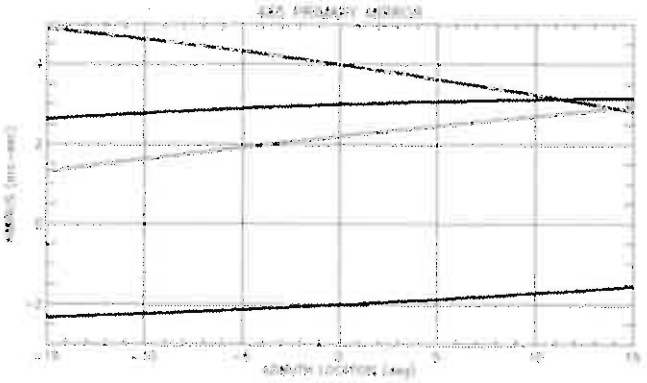

Figure 5. Circumferential centroid components of the Hartmann scans.

Cone-angle error d_1 is calculated from Equation (21). Centroid data at two focal plane locations is required to determine the cone-angle error. The back angle α_0 is calculated from the mirror parameters h_0 and L. After the cone-angle error is known, the average radius error can be calculated using Equation (22).

The residual error, after removing the alignment errors and c-coefficients from the radial components H_{RADIAL}, is the cone-angle variation. Figure 7 plots the retrieved cone angle variation and the cone angle variation of the OSAC model. The developed process retrieves the cone angle variation accurately.

All of the retrieval results are listed in Table 2. The developed retrieval process works very well and finds the error terms accurately. Only 1st-order axial errors (cone-angle variation) were included in the modeling. Third and higher odd-order axial errors could change the determination of the centroids and have an effect on the retrieval process. Second-order axial sag error and higher order axial errors would not affect the centroid calculations because they would distribute the rays equally to both sides of the centroids. Also, large errors could be difficult to model since part of the incoming bundle of rays could only partially hit the surface and have an effect on the centroid calculations.

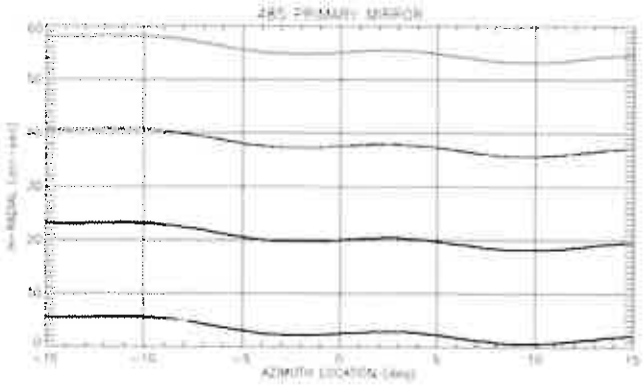

Figure 6. Radial centroid components of the Hartmann scans.

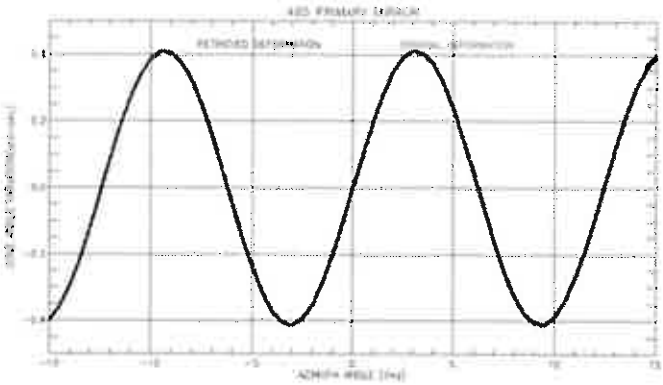

Figure 7. Cone angle variation of the OSAC model and retrieved cone angle variation.

4.2. MODELING OF SECONDARY MIRROR

The secondary mirror is a 30-degree segment of hyperboloid of revolution. The basic parameters of the mirror are given in Table 1. The cone angle variation is modeled using the 21st Legendre -Fourier term:

$$L - F_{21} = constant\ z\ cos(21\theta). \quad (24)$$

The cone-angle variation error is illustrated in Figure 8. The variation has 2 maxima and 2 minima across the azimuth. The axial component is 1st order, or just a constant tilt along the axial direction of the mirror. All of the error parameters are listed in Table 3.

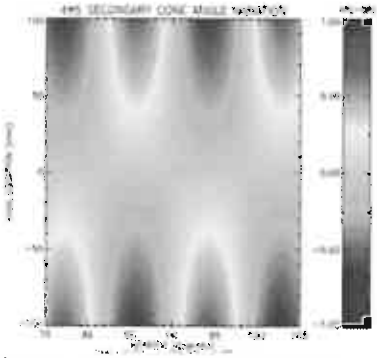

Figure 8. Cone-angle variation model of the secondary mirror.

The secondary mirror is more difficult to model. A collimated beam of rays does not form a perfect on-axis image. Figure 9 plots the footprints of images calculated at 4 focal plane locations. Focal plane locations selected are: best focus, −100 mm, −200 mm, and −300 mm away from the best focus towards the mirror. The best focus is located 5,529.1 mm from the axial center of the mirror. At the best focus the footprint of the image is a bowtie. The bowtie is slightly deformed by the alignment errors and cone-angle variation. The values of these errors are listed in Table 3. Because of the model errors, the top part of the bowtie is smaller than the bottom part. Also, the top edge and bottom edge are not perfect circular arcs. The edges are deformed by the alignment errors and cone-angle variation.

The footprints calculated at larger distances from the best focus are segments of a toroid. The top and bottom edges of the segments are slightly deformed from circular shape by the alignment errors and cone angle variation.

In Figure 10 the centroids of all focal plane locations are plotted. Dashed curves plot the centered centroid profiles and solid curves plot the centroids after they are randomly decentered from their centered locations. Decentered locations are used in the retrieval process.

The centroid curves at out-of-focus locations are long horizontal lines indicating that the defocus term is the dominating error.

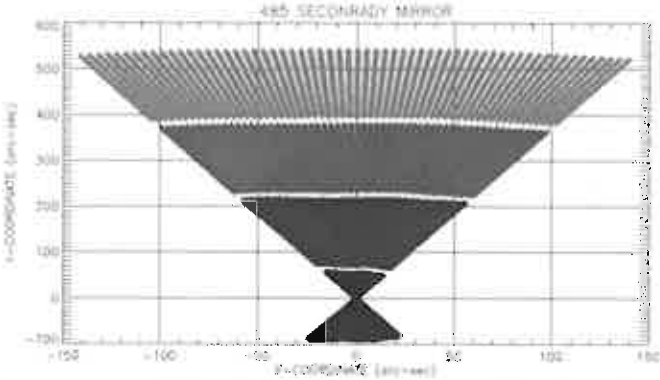

Figure 9. Footprints of the images of secondary mirror at 4 detector locations (best focus, ±100 mm, ±200 mm and ±300 mm from the best focus).

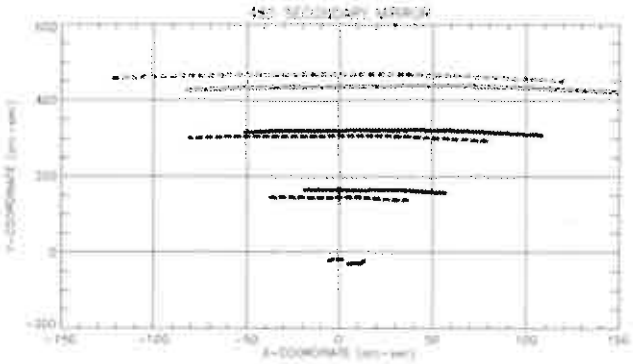

Figure 10. Centroids of 4 Hartmann scans of secondary mirror calculated at best focus ±100 mm, ±200 mm, and ±300 mm from the best focus. Dashed curves represent centered detector centroids and solid curve represents randomly decentered detector centroids.

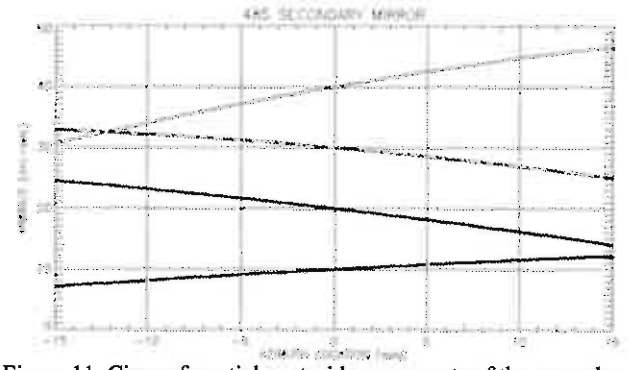

Figure 11. Circumferential centroid components of the secondary mirror.

Table 3. Secondary mirror errors and retrieved errors

	Model error
Elevation alignment error (arc-sec)	-20.00
Azimuth alignment error (arc-sec)	-5.0
Azimuth alignment error of cone angle variation (arc-sec)	-
Average radius error (mm)	0.050
Cone angle error (arc-sec)	10.00
Cone angle variation (arc-sec, PV)	1.38

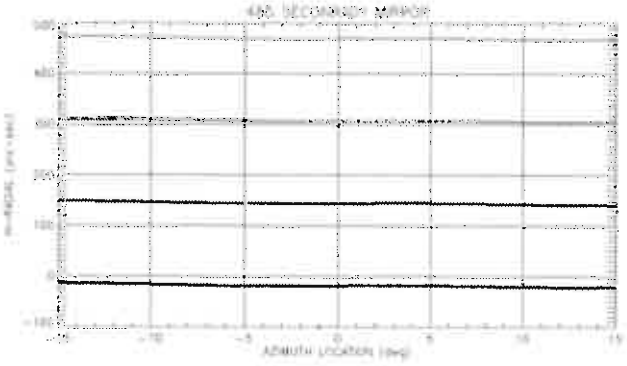

Figure 11 plots the circumferential component (H_{MINUS}) of the centroids as a function of the azimuth angle. The pistons and tilts of the curves are related to the decentering errors x_0 and y_0. In Figure 12 the radial components of the centroids calculated at 4 focal plane locations are plotted. The large vertical separation of the curves indicates that the defocus is dominating the other errors. The slight tilt of the curves is caused by the azimuth alignment

Figure ~~8~~12. Radial centroid components of the secondary mirror.

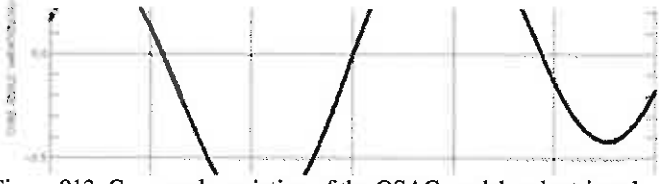

Figure ~~9~~13. Cone angle variation of the OSAC model and retrieved cone angle variation.

errors and the small waviness is caused by the cone-angle variation.

Cone-angle variation of the model is not symmetric along the azimuth range. The error oscillates from a maximum on the left side to a large minimum on the right side. The asymmetry is clearly visible in the surface plot in Figure 8. There is a small amount of azimuth alignment error in this model. A ray trace of the cone-angle variation alone and subsequent retrieval reveals azimuth alignment error of −1.23 arc-sec. The retrieved cone angle variation and the model cone angle variation are plotted in Figure 13. The azimuthal tilt of the model was removed before the variation was plotted.

All of the retrieved errors and errors of the secondary mirror model are listed in Table 3. The developed retrieval process works well in spite of the large on-axis image defect of the secondary mirror.

5. CONCLUSIONS

Highly annular apertures of x-ray Wolter type-1 telescopes make them good candidates for Hartmann testing of circumferential primary and secondary mirror errors, including alignment errors and varying radius and cone-angle errors. On the other hand, this technique would not be practical in measuring axial errors since the radial extent of the surfaces can be just 1-2 mm. If out-of-focus Hartmann scans are done in several focal plane locations, average radius and cone-angle errors, and cone-angle variations can be retrieved. This technique seems an easy way of estimating and assessing these parameters.

Equations (21) and (22) can be used to estimate basic mirror radial parameters h_0, mirror axial focal length L, and back angle α_0 from multiple Hartmann tests. These parameters cannot be measured using conventional normal incidence interferometric techniques that the NGXO project has developed to characterize mirror shape and overall surface quality.

Image-centering techniques can be used to find the image location with respect to the optical axis of the mirror. Through this process one can relate images measured at various detector locations to each other and calculate low-order error parameters or basic parameters of the mirrors.

6. ACKNOWLEDGEMENTS

This work has been financially supported by the Next Generation X-Ray Optics Project at Goddard Space Flight Center in Greenbelt, Maryland.

REFERENCES

[1] Michael P. Biskach, Kai-Wing Chan, Melinda N. Hong, James R. Mazzarella, Ryan S. McClelland, Michael J. Norman, Timo .T. Saha, and William W. Zhang, "Precise alignment and permanent bonding of thin and light weight **x**-ray segments", Proc SPIE, 84433Z (2012).

[2] Tyler C. Evans, Kai-Wing Chan, Ryan McClelland, and Timo Saha, "Arc-Second Alignment and Bonding of International X-Ray Observatory Mirror Segments", Proc SPIE **7732** 77323Z (2010).

[3] Tyler C. Evans, Kai-Wing Chan, Timo T. Saha, "Arc-Second Alignment of International X-Ray Observatory Mirror Segments in a Fixed Structure", Aerospace Conference, 2010 IEEE (2010).

[4] [3] Timo T. Saha, Scott Rohrbach, William W. Zhang, Tyler C. Evans, and Melinda Hong, "Grazing incidence wavefront sensing and verification of x-ray optics performance", Proc SPIE, 814717 (2011).

[5] R.J. Noll, P. Glenn, and J.F. Osantowski, "Optical Surface Analysis Code (OSAC)", Proc. SPIE, **362**, 78 (1983).

[6] Timo T. Saha, "Image Defects from Surface and Alignment Errors in Grazing Incidence Telescopes", Opt. Eng., **29**, 1296 (1990).

[7] Paul Glenn, "Set of Orthonormal Surface Error Descriptors for Near-Cylindrical Optics", Opt. Eng., **23**, 384 (1984).